

Magnetic Transitions in the Chiral Armchair-Kagome System $\text{Mn}_2\text{Sb}_2\text{O}_7$

Darren C. Peets,^{1,2,*} Hasung Sim,^{1,2} Seongil Choi,^{1,2} Maxim Avdeev,³ Seongsu Lee,⁴ Su Jae Kim,⁴ Hoju Kang,⁵ Docheon Ahn,⁵ and Je-Geun Park^{1,2,†}

¹Center for Correlated Electron Systems, Institute for Basic Science (IBS), Seoul 08826, Korea

²Department of Physics and Astronomy, Seoul National University, Seoul 08826, Korea

³Australian Nuclear Science and Technology Organisation, Lucas Heights, NSW 2234, Australia

⁴Neutron Science Division, Korea Atomic Energy Research Institute, Daejeon 34057, Korea

⁵Beamline Department, Pohang Accelerator Laboratory,

80 Jigokro-127-beongil, Nam-gu, Pohang 37673, Gyeongbuk, Korea

(Dated: March 2, 2022)

The competition between interactions in frustrated magnets allows a wide variety of new ground states, often exhibiting emergent physics and unique excitations. Expanding the suite of lattices available for study enhances our chances of finding exotic physics. $\text{Mn}_2\text{Sb}_2\text{O}_7$ forms in a chiral, kagome-based structure in which a fourth member is added to the kagome-plane triangles to form an armchair unit and link adjacent kagome planes. This structural motif may be viewed as intermediate between the triangles of the kagome network and the tetrahedra in the pyrochlore lattice. $\text{Mn}_2\text{Sb}_2\text{O}_7$ exhibits two distinct magnetic phase transitions, at 11.1 and 14.2 K, at least one of which has a weak ferromagnetic component. The magnetic propagation vector does not change through the lower transition, suggesting a metamagnetic transition or a transition involving a multi-component order parameter. Although previously reported in the $P3_121$ space group, $\text{Mn}_2\text{Sb}_2\text{O}_7$ actually crystallizes in $P2$, which allows ferroelectricity, and we show clear evidence of magnetoelectric coupling indicative of multiferroic order. The quasi-two-dimensional ‘armchair-kagome’ lattice presents a promising platform for probing chiral magnetism and the effect of dimensionality in highly frustrated systems.

I. INTRODUCTION

In frustrated magnetic systems, the competition among interactions leads to a rich and sometimes tuneable array of physics, which can be quite subtle and sensitive to perturbations¹. The large and degenerate Hilbert space created in such systems lends itself to a multitude of magnetic ground states and low-lying excited states. Generally, frustration can be introduced *via* competing interactions, such as a balance of direct exchange, superexchange, and Dzyaloshinskii-Moriya interactions, or geometrically, by arranging the magnetic ions in a lattice that prevents a pairwise (anti)ferromagnetic ground state from being simultaneously satisfied within all nearest-neighbour pairs of magnetic atoms. Several such lattices such as pyrochlore, kagome, and triangular are well-known. When new variants of established magnetic lattices are reported, *e.g.* the hyperhoneycomb or tripod-kagome lattices^{2,3}, they offer exciting new playgrounds for the investigation of frustration.

Chiral magnetism in particular offers the possibilities of highly nontrivial long-range magnetic order and topological excitations such as skyrmions⁴. While competing interactions or weak effects such as the Dzyaloshinskii-Moriya interaction^{5,6} can lead to chiral magnetic structures even in the case of an achiral crystal lattice, it may be more natural to expect chiral magnetism to arise if the underlying lattice is itself chiral. The magnetic order may be expected to follow the symmetry of the lattice, even in the absence of the delicate balance of interactions otherwise required, and in many cases all irreducible representations for the magnetic order will be chiral, *constraining* the magnetic order to be chiral by symmetry. Here we

highlight one magnetic material with a novel frustrated lattice in just such a chiral crystal structure.

When prepared by standard high-temperature solid-state synthesis, $\text{Mn}_2\text{Sb}_2\text{O}_7$ forms in a distorted, chiral variant of the trigonal Weberite structure, as shown in Fig. 1⁷⁻⁹. The material’s Mn network is composed of slightly distorted kagome layers in the ab plane, with the kagome triangles linked along the c axis through additional Mn triangle units, such that the simplest structural motif to consider is an Mn_4 armchair unit. Here, we neglect the Sb sublattice, which is known to be non-magnetic Sb^{5+} from ¹²¹Sb Mössbauer spectroscopy¹⁰¹¹. The shortest Mn–Mn bonds in our refinement trace out a helix along the c axis, highlighted in light blue. In the case of a pyrochlore lattice, the atom forming the vertical link would lie directly over the centre of a kagome-layer triangle instead of off to one side, forming a tetrahedron and leading to a highly-symmetric structure in which the faces of the tetrahedra comprise interpenetrating kagome networks. Armchair-kagome $\text{Mn}_2\text{Sb}_2\text{O}_7$ is lower-dimensional, but the interactions both along the c axis and in-plane should exhibit geometric frustration due to the triangular arrangements of Mn atoms. It would be possible, in principle, to deform the Mn sublattice in $\text{Mn}_2\text{Sb}_2\text{O}_7$ into a pyrochlore network through a series of slips perpendicular to the c -axis, but each slip would occur along an entire plane the size of the crystal, and six slips would be required per unit cell, making such a reconstruction enormously energetically unfavorable. This would be a topological transition, since there is one more Mn–Mn link in the pyrochlore’s T_4 tetrahedron than in an Mn_4 armchair¹². The pyrochlore polymorph of $\text{Mn}_2\text{Sb}_2\text{O}_7$, pyr- $\text{Mn}_2\text{Sb}_2\text{O}_7$, also exists but can only be

prepared by a more-difficult low-temperature route^{13–16}. In this paper, ‘ $\text{Mn}_2\text{Sb}_2\text{O}_7$ ’ refers to the armchair-kagome polymorph unless otherwise stated.

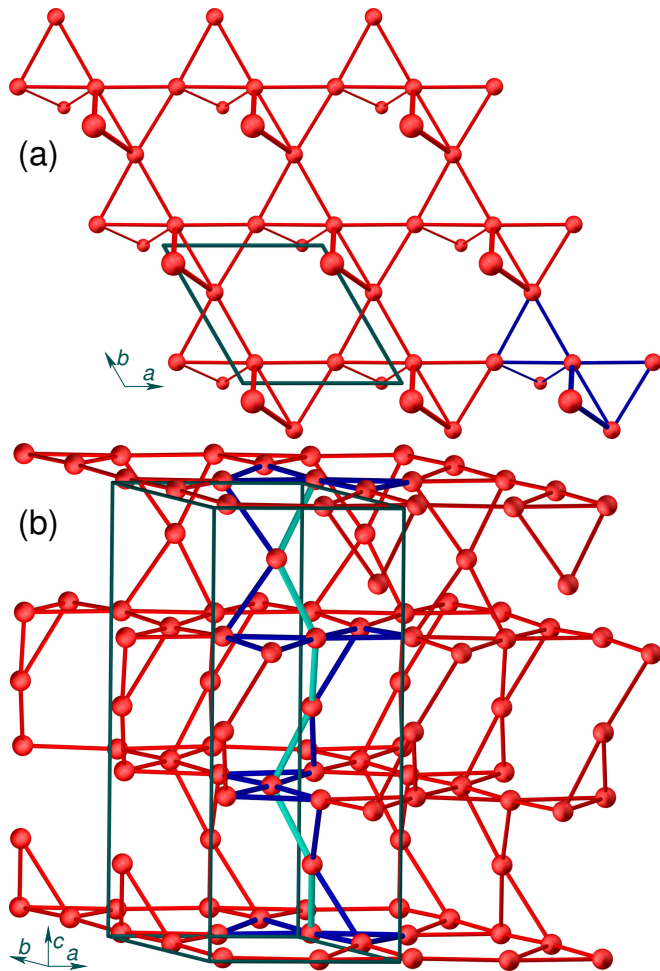


FIG. 1. Manganese sublattice in the $P3_121$ structure of $\text{Mn}_2\text{Sb}_2\text{O}_7$ at 600°C , highlighting the ‘armchair-kagome’ network, based on the refinement in Fig. 10 and Tab. II. (a) Network of armchair units at $z = 0$; one pair of adjacent armchairs is highlighted in blue. (b) The layer stacking leads to a 3-fold screw axis. The stacking sequence of armchair units around the rear corner of the $P3_121$ unit cell is shown in blue, with the shortest bonds in lighter blue. The unit cell is shown using solid lines.

In terms of physical properties, little has been reported on $\text{Mn}_2\text{Sb}_2\text{O}_7$ to date. It has a paramagnetic Curie-Weiss temperature T_{CW} around -45 to -50K with a paramagnetic moment corresponding to high-spin $3d^5$ Mn^{2+} ,¹⁷ and it undergoes a bulk magnetic transition around 13K . The clear history dependence reported below about 55K was attributed to an apparently abrupt onset of short-range correlations. The magnetic structure has not been solved, but most magnetic Bragg peaks could be explained by a $[\frac{1}{2}00]$ propagation vector.¹⁰ ^{121}Sb Mössbauer spectra have been reported¹⁰, but no splitting of the sites was observed, nor any Sb^{3+} component, nor hyperfine

splitting in the magnetically-ordered phase. The material’s isothermal bulk modulus is also known⁹, but the authors are aware of no other measurements.

We set out to clarify the crystal structure and the nature of the magnetic order in $\text{Mn}_2\text{Sb}_2\text{O}_7$, and to check for hints of exotic behavior arising from its unique frustrated chiral lattice. The material forms in an even lower-symmetry structure than that previously reported, and the magnetic order is frustrated, chiral, and multiferroic. $\text{Mn}_2\text{Sb}_2\text{O}_7$ first enters a magnetically-ordered state around 14K in which the magnetization increases rapidly on cooling, followed by a second magnetic transition below which the magnetization saturates.

II. EXPERIMENTAL

Powder samples of $\text{Mn}_2\text{Sb}_2\text{O}_7$ were prepared in Al_2O_3 crucibles in air, from intimately mixed MnO_2 (Alfa Aesar, 99.997%) and Sb_2O_3 (Alfa Aesar, 99.999%). Mixed powders were calcined with intermediate grindings at temperatures between 1050 and 1150°C , typically for 24h per temperature; the mass was monitored for loss of volatile component oxides, and powder diffraction patterns were used to verify phase purity. X-ray powder patterns reported here were collected at temperatures from 30 to 1000°C using a Bruker D8 Discover diffractometer with a $\text{CuK}\alpha$ source. When higher-density samples were desirable, most notably for specific heat and dielectric constant measurements, this powder was pressed isostatically into rods and sintered at 1175°C for a further 24h to produce ceramic.

Magnetization measurements in fields up to 5T were performed in a Quantum Design MPMS-XL SQUID magnetometer in its RSO measurement mode. A powder sample of approximately 15mg was packed inside a gelatin capsule, which was closed with Kapton tape and loaded into a plastic straw. The contribution from the empty sample holder was below the level of the noise on the $\text{Mn}_2\text{Sb}_2\text{O}_7$ data. AC susceptibility measurements were performed in the same magnetometer using the DC sample transport, at zero applied field. Magnetization $M(H)$ data in fields up to 14T were measured using a Quantum Design PPMS with the vibrating sample magnetometry option. Specific heat measurements were performed by the relaxation time method in fields up to 9T in a Quantum Design PPMS, with 2τ fitting and measurement times of 2τ . Sintered ceramic samples were attached to the sample stage using Apiezon N Grease for low-temperature measurements, while Apiezon H Grease was used above $\sim 210\text{K}$ to avoid artifacts from the N Grease glass transition. The addenda contribution was subtracted within the software.

Dielectric measurements were performed at 1kHz using an Andeen-Hagerling AH2550A capacitance bridge. A $3 \times 3\text{mm}^2$, 2mm -thick slab of $\text{Mn}_2\text{Sb}_2\text{O}_7$ ceramic was affixed to a gold backing plate with silver epoxy; a copper wire connected to silver epoxy spread over the opposite

surface completed a capacitor with the $\text{Mn}_2\text{Sb}_2\text{O}_7$ ceramic as its dielectric. This assembly was mounted onto a closed-cycle refrigerator, cooled to ~ 5 K, then measured on warming back to room temperature while the CCR was turned off to reduce noise.

X-ray diffraction found the powder samples to be phase pure for up to $\sim 3\%$ initial cation nonstoichiometry, after two or more calcines above 1050°C . Magnetization measurements, however, proved quite sensitive to the trace presence of Mn_3O_4 , which has a broad ferrimagnetic transition below 50 K^{18,19}. This high sensitivity enabled better optimization of the synthesis conditions than was possible with x-ray diffraction alone. Ultimately, a $\sim 2\%$ antimony excess was used. Samples on which magnetization is presented were additionally washed in citric acid to ensure the complete absence of Mn_3O_4 , although this was later found to be unnecessary. $\text{Mn}_2\text{Sb}_2\text{O}_7$ was also found to be stable in dilute nitric and hydrochloric acids.

A high-resolution synchrotron x-ray powder diffraction pattern was collected at room temperature on beamline 9B (HRPD) at the Pohang Accelerator Laboratory, in Pohang, Korea. A specimen of approximately 0.2 g was prepared by a flat plate side loading method to avoid preferred orientations, and the sample was rotated about the surface normal during the measurement to increase sampling statistics. Data were collected from 10 to 130.5° in steps of 0.005° , using a wavelength of $1.4970(1)$ Å, and they were normalized to the incoming beam intensity and corrected for asymmetric diffraction.

For higher sensitivity to oxygen atoms and to access the magnetic structure, powder neutron diffraction was performed at a variety of temperatures at the ECHIDNA diffractometer at the OPAL research reactor at ANSTO, Australia, from 6.5 to 163.95° in steps of 0.05° , with a neutron wavelength of 2.4395 Å. Low-temperature measurements were performed on loose powder sealed in a vanadium can, while for temperatures above room temperature, the sample was a sintered rod suspended in vacuum. Additional powder neutron diffraction patterns were collected at several temperatures at the high-resolution powder diffractometer (HRPD) at the HANARO research reactor in Daejeon, Korea, from 0 to 159.95° in steps of 0.05° , with a neutron wavelength of 1.8343 Å. To examine the crystal structure with the highest possible resolution, time-of-flight powder neutron diffraction data were also collected at room temperature on the High Resolution Powder Diffractometer (HRPD) at the ISIS spallation neutron source, Rutherford Appleton Laboratory, UK. Data collected on the backscattering (168.33°) and 90° detector banks were used. These data were corrected for self-shielding and wavelength-dependent absorption for a sample with a number density of 2.4×10^{-3} Å⁻³, scattering cross section 41.72 barns, and absorption cross section 36.42 barns at a wavelength of 1.798 Å. Powder diffraction data were Rietveld-refined in FullProf by the least-squares method²⁰.

III. CRYSTAL STRUCTURE

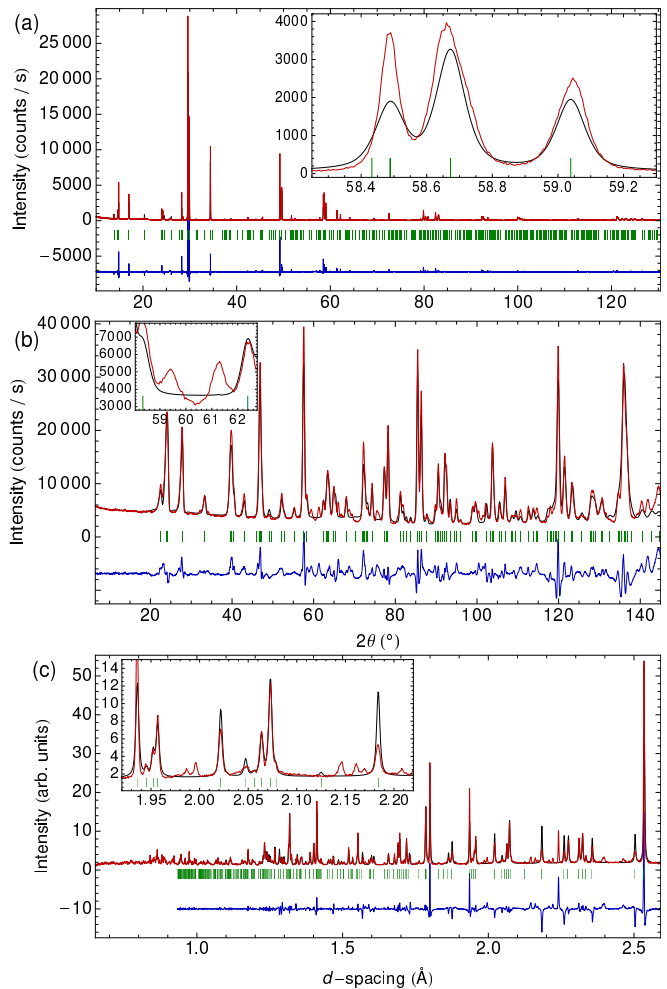


FIG. 2. Powder diffraction patterns of $\text{Mn}_2\text{Sb}_2\text{O}_7$ at 300 K by (a) synchrotron x-ray diffraction, (b) neutron diffraction, and (c) time-of-flight neutron diffraction. Data are in red, the result of refinement within the $P3_121$ structure is shown in black, the residual is in blue, and green vertical bars mark nuclear Bragg positions. The insets highlight illustrative peaks that cannot be well reproduced within $P3_121$. The residuals have been shifted vertically for clarity.

The crystal structure of $\text{Mn}_2\text{Sb}_2\text{O}_7$ has been reported in the $P3_121$ space group ($\#152$)⁷⁻⁹, but there is also a parenthetical remark in the literature that neutron diffraction could only be explained satisfactorily using a doubled unit cell in the $P2$ space group ($\#3$)¹⁷. Our 300 K synchrotron and neutron powder diffraction patterns, shown in Fig. 2, indeed show additional features that cannot be explained within the published $P3_121$ structure. The inset to Fig. 2(a) shows a set of peaks that demonstrate this issue in the synchrotron data — the middle peak is clearly a doublet, but it corresponds to only a single reflection in $P3_121$, while the middle and higher peaks are shifted in opposite directions in a way

that cannot be modelled by any unit cell or geometric adjustments within $P3_121$. The 300 K neutron diffraction pattern in Fig. 2(b) and the time-of-flight data in Fig. 2(c) contain several extra peaks (also see Fig. 3(f)), several of which are shown in the insets. In addition, modeling of peak intensities is poor in all patterns, and this is not resolvable through shifts in atomic positions.

Profile matching in all subgroups of $P3_121$ and various supercells confirmed that the $P2$ space group with a unit cell doubled in-plane was required to explain the observed peak positions. All peaks could be explained within this $P2$ supercell, and impurity phases could not explain the additional peaks. In an independent check, varying the stoichiometry of the starting materials and the calcining conditions had no effect on the putative $P2$ reflections, but a several-percent nonstoichiometry was sufficient to introduce clear impurity peaks at other angles. Attempts to refine the $P2$ structure were not successful — the presumed $P2$ unit cell would have 70 unique atomic sites and almost no symmetry operations to constrain them, so a successful structure refinement will almost certainly require single crystal diffraction data. Based on a refinement of the neutron time-of-flight and synchrotron data with all sites locked to their ideal $P3_121$ positions, the $P2$ cell would have lattice parameters $a = 12.46137(45)$ Å, $b = 7.19304(23)$ Å, $c = 17.40822(30)$ Å, and $\beta = 89.9108(20)^\circ$ (neutron), or $a = 12.45226(15)$ Å, $b = 7.18791(8)$ Å, $c = 17.40312(12)$ Å, and $\beta = 89.92825(83)^\circ$ (synchrotron) at room temperature.

Since the symmetry reduction to $P2$ was clearer in neutron than in synchrotron data, the atomic displacements from high-symmetry positions are likely strongest for oxygen, and one may expect the structure to return to $P3_121$ at high temperature. Diffraction confirmed this — peaks associated with $P2$ gradually weakened upon heating, becoming indistinct around 350°C . Example laboratory x-ray diffraction patterns are shown in Fig. 3(a) and (b); neutron diffraction results are shown in Fig. 3(f). The gradual temperature evolution suggests that this is a second-order displacive transition. Clear evidence for the transition may also be observed in the lattice parameters obtained from refinements within the $P3_121$ structure, shown in Fig. 3(c) and (d). A reduction in the a -axis and an increase in the c -axis lattice parameters relative to a $P3_121$ extrapolation are observed below the transition, estimated from these data as 450°C . The unit cell volume shows no obvious change across the transition. The results of a joint neutron and x-ray refinement in $P3_121$ at 600°C are included in Fig. 10 and Tab. II. The shortest Mn–Mn bond lengths are Mn(1)–Mn(2), which form a helix along the c -axis, while the kagome-plane triangles are not far from equilateral at this temperature.

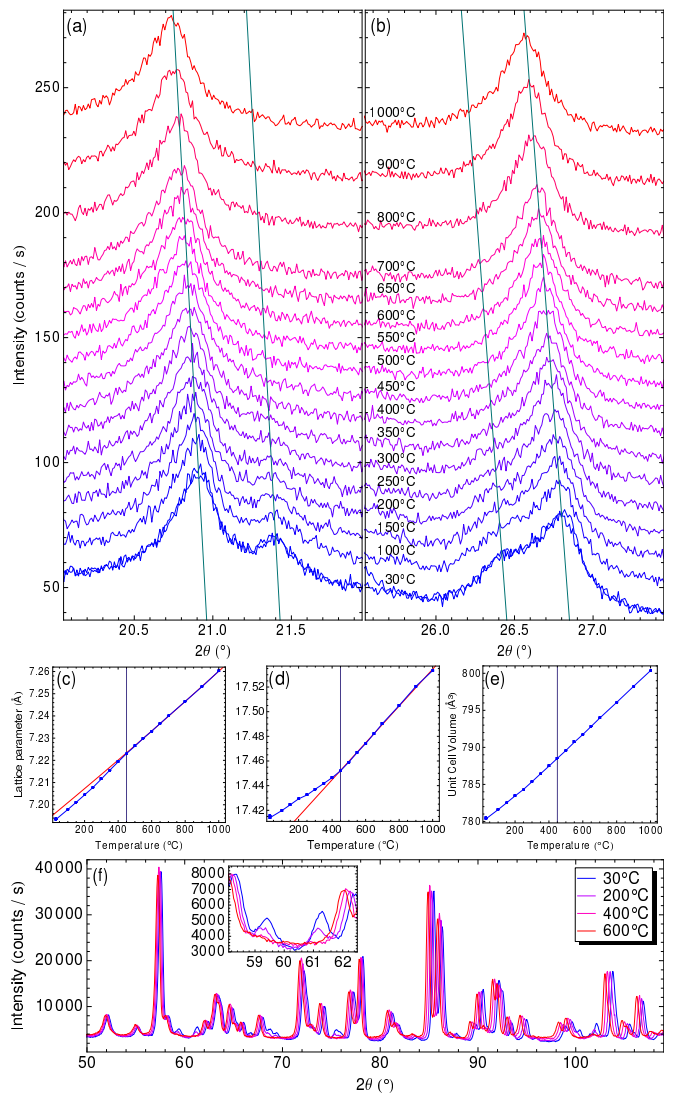


FIG. 3. Transition to $P3_121$ at high temperature. In the laboratory x-ray data in panels (a) and (b), peaks attributable to the $P2$ structure weaken above room temperature, becoming indistinct above 350°C (data sets have been shifted vertically for clarity). The dual traces at 30°C were taken first and last, as an internal check. The (c) a -axis and (d) c -axis lattice parameters show evidence for a transition around 450°C (marked with a vertical line), but there is no clear effect on the (e) unit cell volume. (f) Selected neutron diffraction data: several clear $P2$ -derived peaks vanish above the structural transition — two are highlighted in the inset.

IV. MAGNETIC TRANSITIONS

Among the few physical properties reported on $\text{Mn}_2\text{Sb}_2\text{O}_7$ is magnetization¹⁷. An increase in the magnetization was observed upon cooling through 13 K, taken to be the bulk ordering temperature, while the history-dependence below 55 K was attributed to the onset of short-range correlations. This history dependence was manifested as an approximate doubling of the measured

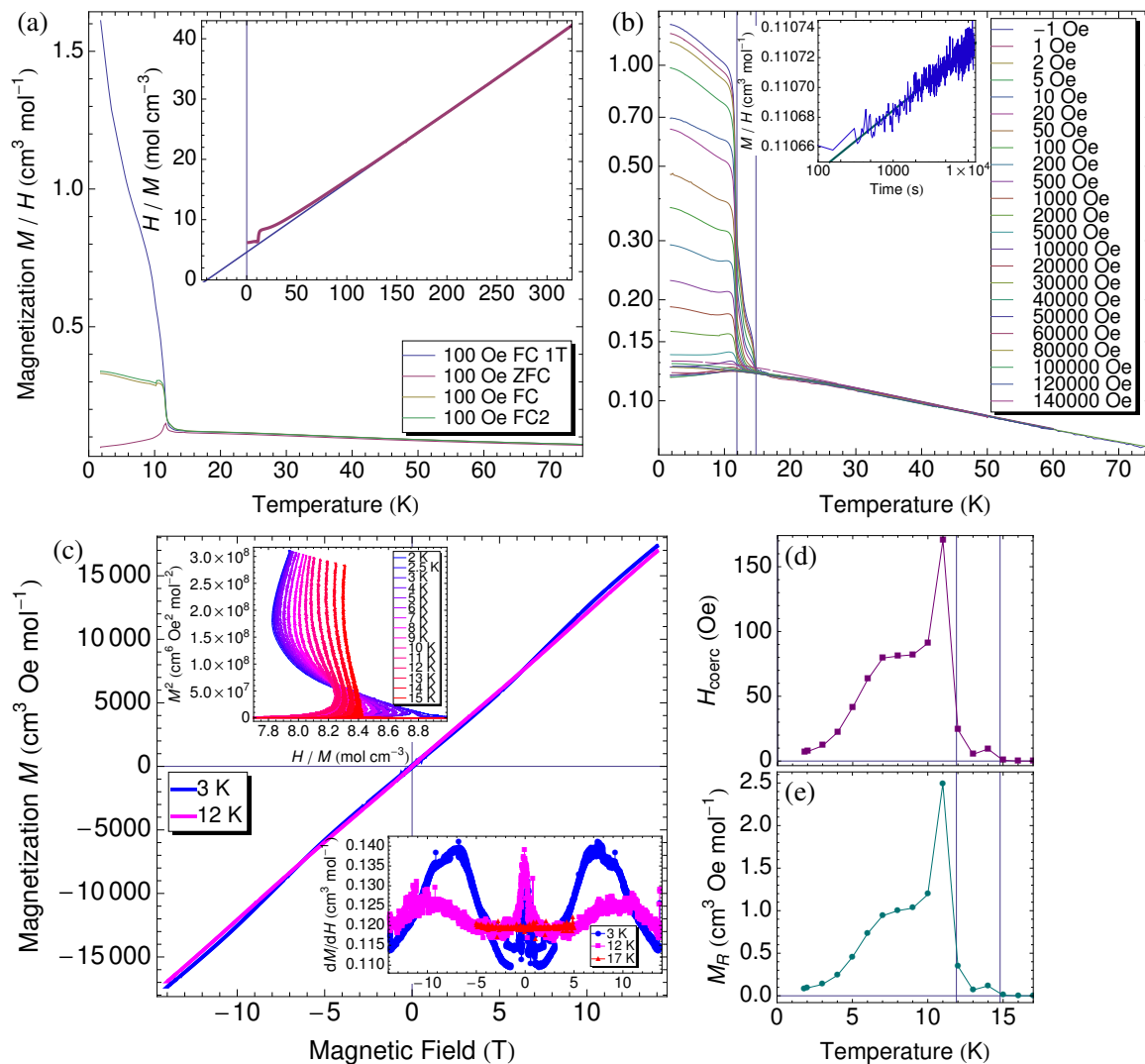


FIG. 4. Low-temperature magnetization of $\text{Mn}_2\text{Sb}_2\text{O}_7$. (a) The field-cooled (FC) magnetization M/H in 100 Oe is compared against zero-field cooled (ZFC) data in the same field, and against data taken on warming in 100 Oe after cooling in an applied field of 1 T as in Ref. 17. The inset shows the inverse magnetization (FC, 2000 Oe), from which a paramagnetic moment of $5.88 \mu_B$ and a Curie-Weiss temperature of -40 K were extracted. (b) Field-cooled magnetization in a variety of fields, plotted on a logarithmic scale. Vertical lines mark the transitions in this sample's specific heat, and the inset shows the result of a relaxation measurement at 1.8 K. (c) $M-H$ loops at 1.8 and 12.75 K, with their derivatives in the lower inset. Below the first transition, there is clear curvature and slight hysteresis. The upper inset is an Arrott plot. The hysteresis in $M(H)$ can be characterized by (d) the coercive field H_{coerc} or (e) the remnant magnetization M_R .

magnetization in the paramagnetic phase under 100 Oe if first cooled in a much higher field¹⁷. Our preliminary magnetization measurements indeed detected a strong history-dependent upturn in magnetization on cooling through a similar temperature range, but this was entirely attributable to ferrimagnetic Mn_3O_4 — the elimination of trace Mn_3O_4 impurities eliminated any features or history dependence above the bulk transition. The magnetization is plotted in Fig. 4(b) with a logarithmic vertical axis to enhance any such weak transition, demonstrating the complete absence of history dependence.

Fig. 4(a) shows data collected as in Ref. 17, as well as zero-field-cooled data. A history-dependence, while ab-

sent above the bulk transition, does appear at low temperatures, indicating some form of magnetically frozen state, a weak ferromagnetic component, or possibly magnetic domains. This would need to be a rather weak ferromagnetic component, since much stronger magnetization jumps were observed from trace ferrimagnetic Mn_3O_4 that was below the detection limit of laboratory x-ray diffraction. The inverse susceptibility, shown in the inset to Fig. 4(a), departs from linearity below ~ 15 K, indicating short-range correlations appearing well ahead of any magnetic order. A fit to the high-temperature inverse susceptibility returns a Curie-Weiss temperature T_{CW} of -40 K and a paramagnetic moment of $5.88 \mu_B$, consis-

tent with the spin-only value for $3d^5$ Mn^{2+} of $5.92 \mu_B$ and with the previous report¹⁷. The onset of short-range correlations well above the transition and the approximate factor of 3 between the Curie-Weiss temperature and the magnetic ordering temperature indicate significant frustration.

The field-cooled magnetization $M(T)$, shown in Fig. 4(a) and (b), shows a striking increase upon cooling through the bulk transition, after which it saturates several Kelvin lower. As will be shown below, these are two separate transitions. The field-dependent magnetization $M(H)$ in Fig. 4(c) is weakly S-shaped with a change in curvature around 7 T, and it shows a slight hysteresis, especially upon entering the $M(T)$ plateau, as can be seen in the temperature dependence of the coercive field H_{coerc} and remnant magnetization M_R in Figs. 4(d) and (e), respectively. The large field dependence in the low-temperature magnetization $M(T)/H$ at low field, when compared with the minor differences in dM/dH (lower inset to Fig. 4(c)), reflect the ferromagnetic component. Changes of slope in dM/dH at 3 K around 6 and 9 T indicate possible metamagnetic transitions, which shift to *higher* fields in the 12 K data. These may have been split or broadened by powder-averaging of the material's presumably anisotropic magnetic properties. That the field scale increases with increasing temperature is somewhat unusual. Arrott plots^{21–24} were also constructed, as shown in the upper inset in Fig. 4c. Near a conventional ferromagnetic transition, these would be linear with a zero intercept. The S-shaped curves here serve to accentuate the changes in curvature in the $M(H)$ data.

One possible explanation for the shape of the $M(T)$ curves could be a transition into a spin state with glassy dynamics, although the temperature dependence of the hysteresis in Figs. 4d and 4e does not take the expected form. To test for relaxation behavior, a sample was cooled to 1.8 K in zero field, the field was increased to 100 Oe, and the decay of the magnetization toward its equilibrium value was then measured. The extremely weak relaxation behavior, visible in the inset to Fig. 4(b), is well described by a single time constant. Present at the parts-per-thousand level at best, this may not be intrinsic. AC susceptometry was also used to check for glassy behavior at the transitions (Fig. 5): the real component of the susceptibility, χ' , shows a sharp feature at the lower transition and a much weaker feature at the upper transition, at temperatures of 11.6 and 14.4 K respectively. There is no frequency dependence to suggest glassy dynamics at the lower transition, while the noise level precludes any definitive pronouncement as to the nature of the upper transition. However, a material would not be expected to enter a glass state upon cooling and then pass through a subsequent phase transition into a long-range ordered state — this would normally be prevented by the glass states's diverging timescale for relaxation. The lower panel of this figure, showing χ'' , contains no hint of an onset in dissipation at either transition.

The low-temperature specific heat of $\text{Mn}_2\text{Sb}_2\text{O}_7$ is

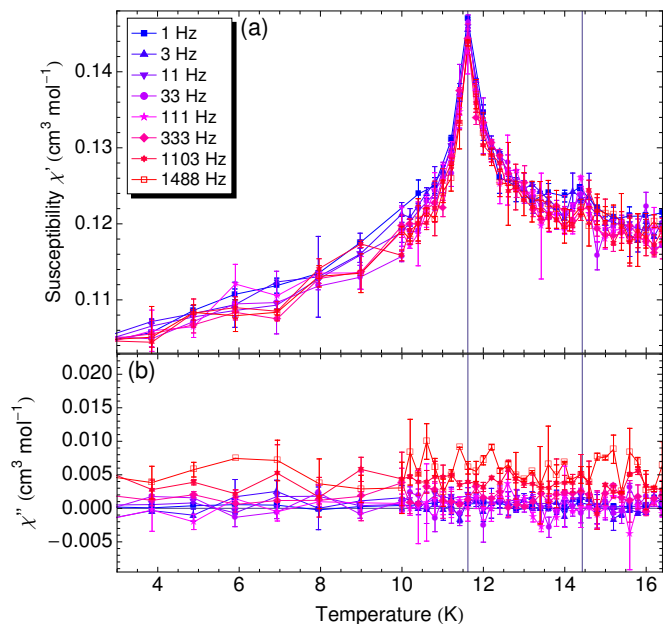


FIG. 5. AC susceptibility of $\text{Mn}_2\text{Sb}_2\text{O}_7$. (a) The real component of the AC susceptibility shows features at both transitions, while the (b) imaginary component is featureless. No frequency dependence or temperature-dependent dissipation was observed. Error bars represent the statistical uncertainty in the fit used to extract each data point.

shown in Fig. 6. Here, two phase transitions are clearly visible, at 11.1 and 14.1 K. Applied fields up to ~ 2 T had no effect, but the peaks began to broaden noticeably by 5 T and became indistinct at higher fields (upper inset). This is likely due to powder averaging of an anisotropic field dependence in the phase transitions. The specific heat implies that the unusual step-and-saturation shape in the temperature-dependent magnetization data actually reflects the onsets of at least two distinct forms of order. Marking the specific heat transitions on the $M(T)$ data in Fig. 4(b) shows that the upper transition corresponds to the first sudden increase in magnetization, while the lower transition coincides roughly with the onset of its saturation.

Examining the specific heat to higher temperatures [lower inset to Fig. 6(a)], one finds a large build-up of magnetic entropy below ~ 40 -50 K. This onset is clearer when the data are plotted as c_P/T , as in the inset to Fig. 6(b). Included for comparison are specific heat data for $\text{Ca}_2\text{Sb}_2\text{O}_7$ and $\text{Sr}_2\text{Sb}_2\text{O}_7$ ²⁵. These form in the closely-related trigonal Weberite structure^{26,27} and are nonmagnetic insulators. $\text{Sr}_2\text{Sb}_2\text{O}_7$ more closely mimics the high-temperature behavior of $\text{Mn}_2\text{Sb}_2\text{O}_7$, but its use as a phonon baseline results in an entropy exceeding the $R \ln 6$ expected for $3d^5$ Mn^{2+} , as shown in Fig. 6(b). This is most likely due to differences in the low-energy phonon spectrum, which would be unsurprising given the Mn version's relaxation into a lower-symmetry $P2$ structure. Mixing of phonons with other types of modes may

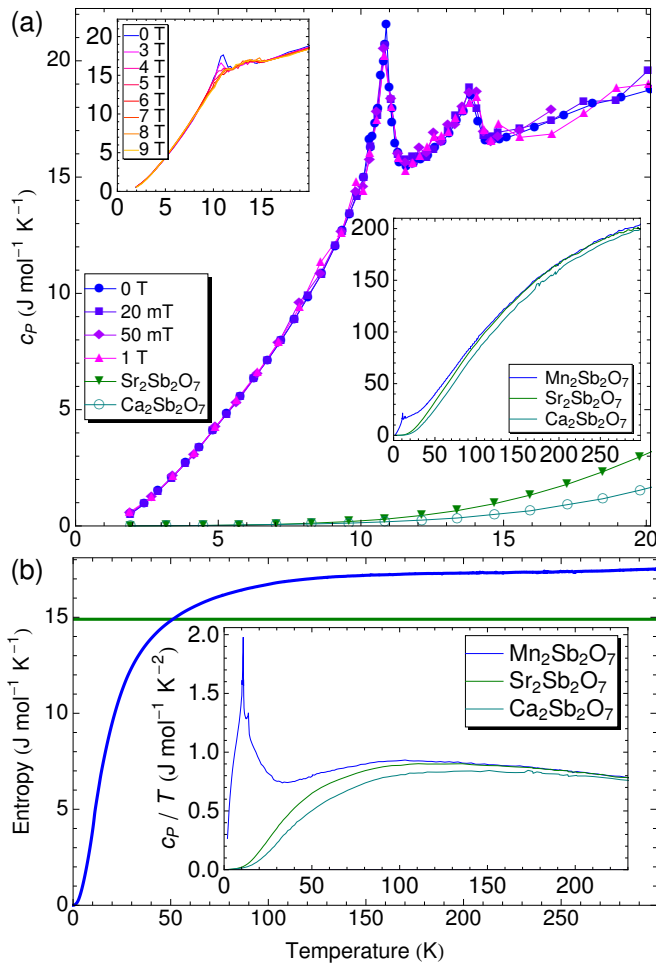


FIG. 6. (a) Low-temperature specific heat of $\text{Mn}_2\text{Sb}_2\text{O}_7$, showing two phase transitions. The upper inset shows high-field behavior on a second sample, while the lower inset shows the high-temperature specific heat at zero field. Nonmagnetic $\text{Sr}_2\text{Sb}_2\text{O}_7$ and $\text{Ca}_2\text{Sb}_2\text{O}_7$ are included for comparison. (b) The accumulated magnetic entropy in $\text{Mn}_2\text{Sb}_2\text{O}_7$ obtained by subtracting that of $\text{Sr}_2\text{Sb}_2\text{O}_7$. The horizontal line marks the $R \ln 6$ expected for $s = 5/2$; the fact that the entropy exceeds this indicates that the phonon subtraction is imperfect. A plot of c_P/T for extracting the magnetic entropy is included in the inset — the phonon contribution in $\text{Mn}_2\text{Sb}_2\text{O}_7$ clearly extends lower in temperature than in the Sr or Ca analogs.

also be a possibility in this space group.

Since the low-temperature $P2$ space group supports ferroelectricity while the $P3_121$ space group does not, multiferroicity is a possibility in this system and measurements of the dielectric properties, shown in Fig. 7, can provide further insight into the phase transitions. The capacitance shows a sharp downturn at the upper magnetic transition, where the magnetic order locking-in reduces the material's ability to electrically polarize (and store energy as a dielectric). A corresponding peak in the dissipation factor is attributed to order parameter fluctuations near the transition. The appearance of such fluctuations for a magnetic transition in an elec-

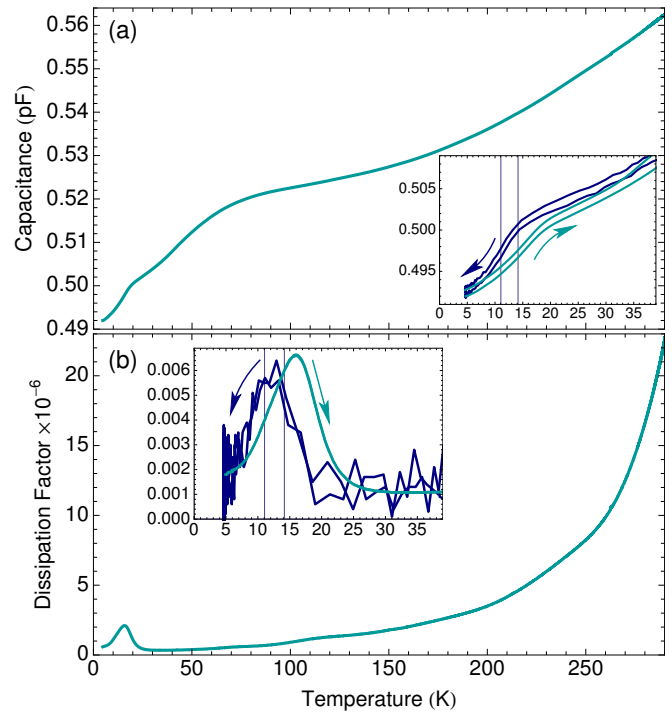


FIG. 7. Temperature dependence of the (a) capacitance and (b) dissipation factor when $\text{Mn}_2\text{Sb}_2\text{O}_7$ is employed as the dielectric in a capacitor. The insets show multiple warming and more-rapid cooling runs, with the specific heat transitions marked for reference.

trostatic quantity implies multi-component order. The capacitance undergoes a broader but stronger reduction centered around 50 K, with no corresponding peak in the dissipation factor. This represents the onset of short-range magnetic order and matches well with the heat capacity estimate. Above ~ 100 K, where magnetism plays no significant role, the reduction in the capacitance (and thus polarizability) upon cooling is suggestive of a tendency toward antiferroelectric order below the structural transition, in much the same way that a reduction in magnetic susceptibility is seen below a pure antiferromagnetic transition.

Data were collected on free warming to minimize noise, and $\text{Mn}_2\text{Sb}_2\text{O}_7$'s specific heat is very large at low temperatures, so the sample temperature lags the thermometry leading to an apparent shift of the data to slightly higher temperatures. To confirm that the upper transition is indeed the electrically-active one, data taken upon cooling with a sweep rate roughly an order of magnitude faster are included in the insets to Fig. 7. All observed features remain above the lower transition, unambiguously identifying the upper transition as the electrically active one.

The clear detection of a magnetic transition and its order parameter fluctuations in bulk electrostatic properties implies strong magnetoelectric coupling and mixed-character (multiferroic) order parameters. It also confirms that the space group supports ferroelectricity, lend-

ing additional support to the assignment of $P2$.

V. MAGNETIC STRUCTURE

TABLE I. Magnetic reflections in $\text{Mn}_2\text{Sb}_2\text{O}_7$. Observed and calculated d -spacings in \AA based on data from both ANSTO and HANARO, approximate relative intensities (Rel. Int.), and index in $P3_121$ and $P2$ of the observed magnetic peaks are listed.

$P3_121$	$P2$	d	d_{HANARO}	d_{calc}	Rel. Int.
$(\frac{1}{2}00)$	(100)	12.44	—	12.43	3.9
$(\frac{1}{2}01)$	(101)	10.15	—	10.12	2.6
$(\frac{1}{2}02)/(\frac{1}{2}10)$	(102)/(010)	7.15	7.06	7.13	27
$(\frac{1}{2}11)$	(011)	6.65	6.55	6.64	24
$(\frac{1}{2}12)$	(012)	5.53	5.47	5.53	23
$(\frac{1}{2}03)$	(103)	5.26	5.20	5.25	39
$(\frac{3}{2}10)$	(210)	4.68	4.65	4.70	33
$(\frac{3}{2}11)$	(211)	4.53	4.48	4.53	100
$(\frac{3}{2}00)/(\frac{3}{2}12)$	(212)	4.13	4.08	4.13	24
$(\frac{3}{2}01)$	(301)	4.03	—	4.03	9.8
$(\frac{1}{2}14)/(\frac{3}{2}02)$	(014)/(302)	3.71	3.66	3.72	31
$(\frac{3}{2}21)/(\frac{3}{2}03)$	(121)/(303)	3.38	3.36	3.38	26
$(\frac{5}{2}10)$	(410)	2.85	2.84	2.85	4.9
$(\frac{1}{2}06)/(\frac{5}{2}11)$	(106)/(411)	2.81	2.80	2.81	11
$(\frac{1}{2}16)/(\frac{5}{2}21)$	(016)/(321)	2.68	2.66	2.68	17
several	several	2.21	2.20		23
several	several	2.20	2.19		6.6
several	several	1.88	1.88		14

Neutron diffraction was performed through both magnetic transitions — data in the relevant temperature range appear in Fig. 8(a). Fig. 8(b) shows the same data after subtraction of a pattern taken at 17 K, just above the upper magnetic transition. All magnetic peaks can be qualitatively explained by a propagation vector of $(\frac{1}{2}00)$ in the $P3_121$ unit cell, or (000) in the larger $P2$ cell, as summarized in Tab. I. Since the underlying $P2$ crystal structure could not be refined, and since the number of observed magnetic peaks is similar to the expected number of Mn sites, refinement of the magnetic structure was not completed. The $P2$ space group supports two irreducible representations for the magnetic order, both of which are chiral, and it was not possible to distinguish between them. Calculated d -spacings in Tab. I are based on the $P2$ assignments. Based on the limited data, it appears that peaks with $h+k=\text{odd}$ in $P2$ are favored.

As has previously been reported¹⁷, there is a significant diffuse peak centered around a d -spacing of 5 \AA , and 2 \AA wide — see Fig. 8(c). Comparison to 300 K data indicated that this feature is essentially absent above 70 K, so data collected at 100 K were used as a baseline for subtraction. The appearance of the diffuse peak around 50-70 K provides further evidence for the onset of local

spin correlations around that temperature. Its intensity reaches a maximum between the two magnetic transitions, and then the magnetic intensity is transferred into the magnetic Bragg peaks at low temperatures.

The temperature dependence of the magnetic peaks is shown in Figs. 8(d) and 8(e). The intensity falls off as would be expected for a second-order transition at 11 K, but a small fraction of the intensity persists to the higher magnetic transition. The magnetic peaks in both phases are located at the same angles and can be described by the same shape parameters and intensity ratios, although the low intensity between the two transitions makes firm conclusions difficult. The strong similarity indicates that the two magnetic phases are closely related — perhaps distinguished by a canting angle, stacking along the hexagonal c axis, or coupling to antiferroelectric order.

VI. DISCUSSION AND CONCLUSION

As is clear from the magnetization, specific heat and neutron diffraction data, $\text{Mn}_2\text{Sb}_2\text{O}_7$ undergoes two magnetic phase transitions at low temperature. The upper transition is multiferroic in nature, while the lower is purely magnetic. Below the lower transition, the magnetization saturates and the hysteresis reaches its maximum before subsiding, suggesting that the ground state is some form of global antiferromagnetic order. Between the two transitions, the magnetization increases sharply upon cooling, implying a small net moment. The temperature-dependence of the apparent high-field transitions in $M(H)$ suggests frustration is relieved by the field.

The magnetic sublattice is intermediate between two-dimensional kagome and three-dimensional pyrochlore, so this material offers a platform for interpolating between two- and three-dimensional frustrated magnetism. The clearest comparison to a pyrochlore system is to the pyrochlore polymorph of $\text{Mn}_2\text{Sb}_2\text{O}_7$ itself¹³⁻¹⁶. This latter structural variant has only been successfully prepared *via* a specific low-temperature route, substituting Mn^{2+} into the pre-existing pyrochlore Sb^{5+} framework of $\text{Sb}_2\text{O}_5 \cdot n\text{H}_2\text{O}$ ($n \sim 1.5-2$). By having 6 Mn-Mn links within a tetrahedron rather than five within an armchair unit, one might expect the pyrochlore's Curie-Weiss temperature to be 20% stronger, or -48 K. Experimentally, we found it to be -49 K¹⁶. One would also expect a significantly higher frustration factor $f \equiv T_{\text{CW}}/T_{\text{N}}$ in the pyrochlore, and again this is exactly what we observe: $f_{\text{ak}} = 2.8$ for the armchair-kagome structure and $f_{\text{pyr}} = 9.0$ for the pyrochlore. The stronger frustration in the pyrochlore polymorph leads to a spin-glass ground state, rather than the three-dimensional magnetic order observed here.

For a more direct comparison, temperature-dependent magnetization data are plotted in unitless form for both polymorphs in Fig. 9, obtained by rearranging the Curie-

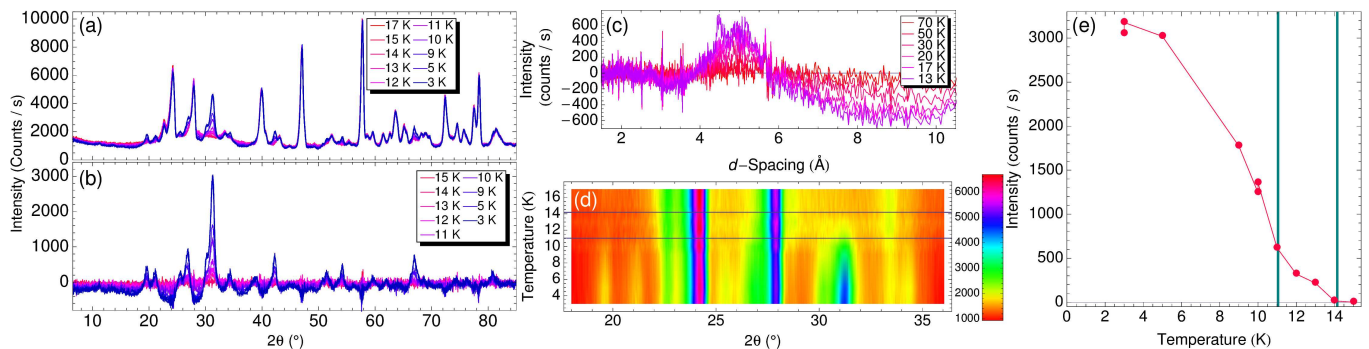


FIG. 8. Magnetic intensity at low temperature. (a) Diffraction patterns at various temperatures. (b) Difference with respect to 17 K, to highlight the magnetic peaks. (c) A significant diffuse peak is visible above the transition around a d -spacing of 5 Å when data taken at 100 K are used for subtraction. Panels (d) and (e) demonstrate that while much of the intensity in these peaks vanishes at the lower magnetic transition, some persists to the upper transition.

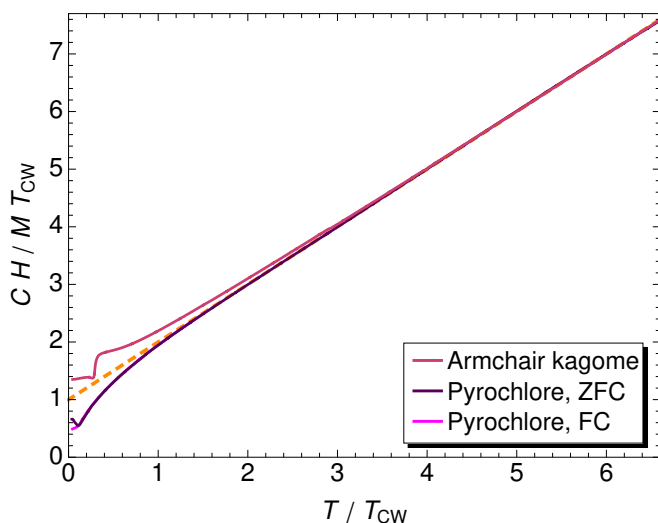


FIG. 9. Comparison of the armchair-kagome and pyrochlore variants of $\text{Mn}_2\text{Sb}_2\text{O}_7$. Magnetization data on the former polymorph were taken at 2000 Oe (field-cooled), and are the same data as in the Fig. 4a inset. Data on the pyrochlore were taken at 100 Oe under field-cooled and zero-field-cooled conditions¹⁶.

Weiss law $M/H = C/(T - T_{\text{CW}})$ as $CH/MT_{\text{CW}} = T/T_{\text{CW}} - 1$ ²⁸. Data above the dashed line indicate additional antiferromagnetic interactions, while points can be pushed below the line by ferromagnetic interactions. Deviations from ideal Curie-Weiss behavior start at a higher fraction of T_{CW} in the armchair-kagome structure and indicate additional antiferromagnetic fluctuations, whereas the deviations from Curie-Weiss behavior in the pyrochlore are ferromagnetic. The transitions in both polymorphs lie well below the unfrustrated $T_{\text{N}} = T_{\text{CW}}$.

In summary, we have shown that the structure of $\text{Mn}_2\text{Sb}_2\text{O}_7$ must be $P2$ under ambient conditions, but that it returns to the higher-symmetry $P3_121$ structure above $\sim 450^\circ\text{C}$ in an apparent second-order displacive transition. Solving the $P2$ modification will most likely

require single crystals. The armchair-kagome network seen in the $P3_121$ structure has not, to our knowledge, been modeled theoretically, and investigation of its possible magnetic and multiferroic ground states as a function of interaction strengths would be an interesting and fruitful topic for future research. The Mn_4 armchair units constitute an intermediate case between the two-dimensional triangular network of the kagome lattice and the fully three-dimensional tetrahedra of the pyrochlore, and likely support their own unique suite of ground states as a function of the exchange parameters. Interestingly, the smaller Sb^{5+} ions form identical structural armchair motifs, but with an additional twist between layers that is not present in the Mn sublattice. It would be worthwhile to explore the possibility of putting magnetic ions on this site instead.

Magnetic Bragg peaks are consistent with a propagation vector of $(\frac{1}{2}00)$ in $P3_121$ or (000) in $P2$, but a magnetic structure could not be refined. Because the latter crystal structure only supports chiral irreducible representations for the magnetic order, we infer that the magnetic order in the material is chiral. Chiral magnetism can lead to a variety of exotic physics, and will be of significant interest for its excitations and field-dependence. The possibility of skyrmion-like excitations⁴ in a system with chiral multiferroic order would be particularly enticing, as it would enable control and manipulation of the magnetism and excitations through standard electronic means. In the closely-related MnSb_2O_6 ²⁹, the novel cycloidal magnetic order has been predicted to lead to a unique ferroelectric switching mechanism, while the material should behave in an analogous way to ferroaxial multiferroics³⁰, and it would be interesting to determine whether similar physics could be available here. $\text{Mn}_2\text{Sb}_2\text{O}_7$ has some key differences, however, and may host its own suite of entirely unique physics.

ACKNOWLEDGEMENTS

This work was supported by the Institute for Basic Science (IBS) in Korea (IBS-R009-G1), and work at HANARO was supported by the Nuclear R&D Program through NRF Grant No. 2012M2A2A6002461. The authors are indebted to M. Gingras, D.I. Khomskii, M.J.

Lawler, M.D. Le, and Y. Noda for stimulating discussions, the NCIRF for assistance with several measurements, and K.S. Knight at ISIS for assistance with the time-of-flight diffraction measurement. We acknowledge the support of the Bragg Institute, Australian Nuclear Science and Technology Organisation, in providing neutron research facilities used in this work.

-
- * dpeets@fudan.edu.cn; Current address: Advanced Materials Laboratory, Fudan University, Shanghai 200438, China
- † jgpark10@snu.ac.kr
- ¹ C. Lacroix, P. Mendels, and F. Mila, eds., *Introduction to Frustrated Magnetism*, Springer Series in Solid-State Sciences, Vol. 164 (Springer, Berlin, 2011).
 - ² T. Takayama, A. Kato, R. Dinnebier, J. Nuss, H. Kono, L. S. I. Veiga, G. Fabbris, D. Haskel, and H. Takagi, *Phys. Rev. Lett.* **114**, 077202 (2015), arXiv:1403.3296 [cond-mat.str-el].
 - ³ Z. Dun, J. Trinh, K. Li, M. Lee, K.-W. Chen, R. Baumbach, Y. Hu, Y. Wang, E. S. Choi, B. S. Shastry, A. P. Ramirez, and H. Zhou, *Phys. Rev. Lett.* **116**, 157201 (2016), arXiv:1601.01575 [cond-mat.str-el].
 - ⁴ S. Mühlbauer, B. Binz, F. Jonietz, C. Pfleiderer, A. Rosch, A. Neubauer, R. Georgii, and P. Böni, *Science* **323**, 915 (2009), arXiv:0902.1968 [cond-mat.str-el].
 - ⁵ I. Dzyaloshinsky, *J. Phys. Chem. Solids* **4**, 241 (1958).
 - ⁶ T. Moriya, *Phys. Rev.* **120**, 91 (1960).
 - ⁷ H. G. Scott, *J. Solid State Chem.* **66**, 171 (1987).
 - ⁸ H. G. Scott, *Z. Kristallogr.* **190**, 41 (1990).
 - ⁹ L. Chelazzi, T. B. Ballaran, G. O. Lepore, L. Bindi, and P. Bonazzi, *Solid State Sci.* **21**, 85 (2013).
 - ¹⁰ M. A. Subramanian, A. Clearfield, A. M. Umarji, and G. K. Shenoy, *J. Solid State Chem.* **52**, 124 (1984).
 - ¹¹ Ref. 10 describes the crystal structure as rhombohedrally-distorted pyrochlore — the correct space group had not yet been identified. The samples were prepared by a high-temperature route that produces the trigonal Weberite structure investigated here¹⁷.
 - ¹² C. L. Kane and T. C. Lubensky, *Nat. Phys.* **10**, 39 (2013), arXiv:1308.0554 [cond-mat.mes-hall].
 - ¹³ F. Brisse, D. J. Stewart, V. Seidl, and O. Knop, *Can. J. Chem.* **50**, 3648 (1972).
 - ¹⁴ H. D. Zhou, C. R. Weibe, A. Harter, N. S. Dalal, and J. S. Gardner, *J. Phys.: Condens. Matter* **20**, 325201 (2008).
 - ¹⁵ H. D. Zhou, C. R. Weibe, J. A. Janik, B. Vogt, A. Harter, N. S. Dalal, and J. S. Gardner, *J. Solid State Chem.* **183**, 890 (2010).
 - ¹⁶ D. C. Peets, H. Sim, M. Avdeev, and J.-G. Park, *Phys. Rev. B* **94**, 174431 (2016), arXiv:1611.02811 [cond-mat.str-el].
 - ¹⁷ J. N. Reimers, J. E. Greedan, C. V. Stager, M. Bjorgvinnsen, and M. A. Subramanian, *Phys. Rev. B* **43**, 5692 (1991).
 - ¹⁸ K. Dwight and N. Menyuk, *Phys. Rev.* **119**, 1470 (1960).
 - ¹⁹ G. B. Jensen and O. V. Nielsen, *J. Phys. C: Solid State Phys.* **7**, 409 (1974).
 - ²⁰ J. Rodríguez-Carvajal, *Physica B* **192**, 55 (1993).
 - ²¹ K. P. Belov and A. N. Goryaga, *Fiz. Met. Metalloved.* **2**, 3 (1956).
 - ²² A. Arrott, *Phys. Rev.* **108**, 1394 (1957).
 - ²³ A. Arrott and J. E. Noakes, *Phys. Rev. Lett.* **19**, 786 (1967).
 - ²⁴ S. Bustingorry, F. Pomiro, G. Aurelio, and J. Curiale, *Phys. Rev. B* **93**, 224429 (2016), and references therein.
 - ²⁵ O. Knop, G. Demazeau, and P. Hagenmuller, *Can. J. Chem.* **58**, 2221 (1980).
 - ²⁶ W. Verscharen and D. Babel, *J. Solid State Chem.* **24**, 405 (1978).
 - ²⁷ L. Cai and J. C. Nino, *Acta Crystallogr.* **B65**, 269 (2009).
 - ²⁸ S. E. Dutton, E. D. Hanson, C. L. Broholm, J. S. Slusky, and R. J. Cava, *J. Phys.: Condens. Matter* **23**, 386001 (2011).
 - ²⁹ J. N. Reimers, J. E. Greedan, and M. A. Subramanian, *J. Solid State Chem.* **79**, 263 (1989).
 - ³⁰ R. D. Johnson, K. Cao, L. C. Chapon, F. Fabrizi, N. Perks, P. Manuel, J. J. Yang, Y. S. Oh, S.-W. Cheong, and P. G. Radaelli, *Phys. Rev. Lett.* **111**, 017202 (2013), arXiv:1306.3854 [cond-mat.str-el].

Appendix A: High-Temperature $P3_121$ Structure Refinement

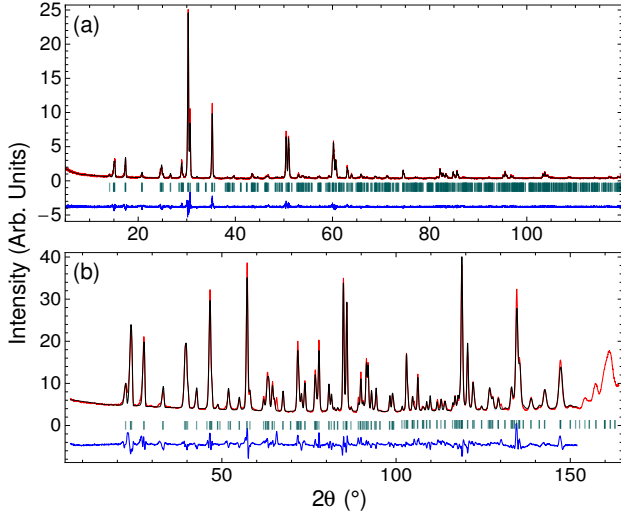


FIG. 10. Joint refinement of (a) x-ray and (b) neutron powder diffraction data at 600°C in the $P3_121$ space group (#152). Data are in red, the fit is in black, the residual is in blue, and vertical bars mark the calculated Bragg positions. The residuals have been shifted for clarity.

TABLE II. Refined atomic positions in the $P3_121$ space group (#152) at 600°C, well above the structural transition, from a joint refinement of x-ray and neutron powder diffraction patterns. $a = 7.22277(7)$ Å and $c = 17.4479(2)$ Å in the neutron pattern and $a = 7.2248(2)$ Å and $c = 17.4545(7)$ Å in the x-ray pattern. The overall R -factors based on all points and not corrected for background are $R_p = 5.92\%$ and $R_{wp} = 7.88\%$ for the neutron pattern and $R_p = 8.84\%$ and $R_{wp} = 11.6\%$ for the x-ray pattern, based on 202 neutron reflections and 1199/2 reflections for the x-ray pattern.

Atom	Mult	x	y	z	B_{iso}
Mn(1)	3a	0.853(4)	0	0.33333	3.09(18)
Mn(2)	3b	0.868(3)	0	0.83333	3.09(18)
Mn(3)	6c	0.659(3)	0.152(4)	-0.0039(8)	3.09(18)
Sb(1)	3a	0.3227(16)	0	0.33333	0.78(10)
Sb(2)	3b	0.3387(19)	0	0.83333	0.78(10)
Sb(3)	6c	0.4953(22)	0.3361(20)	0.1646(5)	0.78(10)
O(1)	6c	0.1954(17)	0.2235(14)	0.1408(5)	1.78(7)
O(2)	6c	0.5617(10)	0.6161(15)	0.1987(5)	1.78(7)
O(3)	6c	0.1905(16)	0.6366(16)	0.1437(5)	1.78(7)
O(4)	6c	-0.0446(12)	0.3105(18)	0.0540(3)	1.78(7)
O(5)	6c	-0.0396(10)	0.8045(20)	0.0555(4)	1.78(7)
O(6)	6c	0.5395(21)	0.4016(12)	0.0554(4)	1.78(7)
O(7)	6c	0.5499(15)	0.8179(20)	0.0597(4)	1.78(7)

Figure 10 and Tab. II report the result of a joint refinement of x-ray and neutron powder diffraction data in the high-temperature $P3_121$ structure (space group

#152) at 600°C. B_{iso} parameters were constrained to be the same on all sites for each element. The lattice parameters at this temperature were found to be $a = 7.22277(7)$ Å and $c = 17.4479(2)$ Å in the neutron pattern and $a = 7.2248(2)$ Å and $c = 17.4545(7)$ Å in the x-ray pattern. The overall R -factors based on all points and not corrected for background were $R_p = 5.91\%$ and $R_{wp} = 7.87\%$ for the neutron pattern and $R_p = 8.58\%$ and $R_{wp} = 11.3\%$ for the x-ray pattern, based on 202 neutron reflections and 1199/2 reflections in the x-ray pattern. The resulting Mn–Mn bond lengths and bond angles are summarized in Tab. III. At least at this temperature, the kagome planes are much closer to their ideal shape than in the previously-reported structure refinement⁸. It is not clear whether this is due to the elevated temperature, the sample quality, or the previous use of the high-temperature space group at room temperature.

TABLE III. Mn–Mn distances and Mn–Mn–Mn angles in $P3_121$ $\text{Mn}_2\text{Sb}_2\text{O}_7$ (space group #152) at 600°C, for the refinement reported in Tab. II and Fig. 10. Mn(2) is the site linking adjacent kagome planes, Mn(1) has bonds to two out-of-plane Mn(2) atoms, and the two Mn(3) atoms each have a bond to only one out-of-plane Mn(2) atom.

Atom 1	Atom 2	Atom 3	Bond length (Å)	Angle (°)
Mn(1)	Mn(2)		3.393(16)	
Mn(1)	Mn(3)		3.54(3)	
Mn(1)	Mn(3)		3.68(2)	
Mn(2)	Mn(3)		3.64(2)	
Mn(3)	Mn(3)		3.62(3)	
Mn(2)	Mn(1)	Mn(2)		126.1(4)
Mn(2)	Mn(1)	Mn(3)		63.2(7)
Mn(2)	Mn(1)	Mn(3)		115.1(10)
Mn(2)	Mn(1)	Mn(3)		92.1(7)
Mn(2)	Mn(1)	Mn(3)		90.3(7)
Mn(3)	Mn(1)	Mn(3)		177.6(16)
Mn(3)	Mn(1)	Mn(3)		60.0(9)
Mn(3)	Mn(1)	Mn(3)		121.0(12)
Mn(3)	Mn(1)	Mn(3)		119.0(11)
Mn(1)	Mn(2)	Mn(1)		128.1(4)
Mn(1)	Mn(2)	Mn(3)		60.5(8)
Mn(1)	Mn(2)	Mn(3)		171.4(8)
Mn(3)	Mn(2)	Mn(3)		111.0(8)
Mn(1)	Mn(3)	Mn(1)		177.6(16)
Mn(1)	Mn(3)	Mn(2)		125.3(11)
Mn(1)	Mn(3)	Mn(2)		56.4(8)
Mn(1)	Mn(3)	Mn(3)		58.1(9)
Mn(1)	Mn(3)	Mn(3)		119.0(11)
Mn(1)	Mn(3)	Mn(3)		120.8(12)
Mn(1)	Mn(3)	Mn(3)		61.9(9)
Mn(2)	Mn(3)	Mn(3)		95.8(8)
Mn(2)	Mn(3)	Mn(3)		89.3(8)
Mn(3)	Mn(3)	Mn(3)		174.9(10)